Geophysical Research Letters

RESEARCH LETTER
10.1029/2018GL080997

Complex and Diverse Rupture Processes of the 2018 *Mw* 8.2 and *Mw* 7.9 Tonga-Fiji Deep Earthquakes

Wenyuan Fan[1,2], S. Shawn Wei[3], Dongdong Tian[3], Jeffrey J. McGuire[2], and Douglas A. Wiens[4]

[1]Department of Earth, Ocean and Atmospheric Science, Florida State University, Tallahassee, FL, USA, [2]Department of Geology and Geophysics, Woods Hole Oceanographic Institution, Woods Hole, MA, USA, [3]Department of Earth and Environmental Sciences, Michigan State University, East Lansing, MI, USA, [4]Department of Earth and Planetary Sciences, Washington University, Saint Louis, MO, USA

Key Points:
- The *Mw* 8.2 Tonga earthquake ruptured for 37 s at 4.1 km/s and likely propagated from the cold slab core to warmer surrounding regions
- The *Mw* 8.2 Tonga earthquake excited high-frequency seismic radiation spatially coinciding with abundant aftershocks
- The *Mw* 7.9 Fiji earthquake was dynamically triggered in a previously aseismic region and ruptured for 35 s at 2.5 km/s likely through a dissipative process

Supporting Information:
- Supporting Information S1

Correspondence to:
W. Fan,
wfan@fsu.edu

Citation:
Fan, W., Wei, S. S., Tian, D., McGuire, J. J., & Wiens, D. A. (2019). Complex and diverse rupture processes of the 2018 *Mw* 8.2 and *Mw* 7.9 Tonga-Fiji deep earthquakes. *Geophysical Research Letters*, *46*. https://doi.org/10.1029/2018GL080997

Received 19 OCT 2018
Accepted 15 FEB 2019
Accepted article online 20 FEB 2019

Abstract Deep earthquakes exhibit strong variabilities in their rupture and aftershock characteristics, yet their physical failure mechanisms remain elusive. The 2018 *Mw* 8.2 and *Mw* 7.9 Tonga-Fiji deep earthquakes, the two largest ever recorded in this subduction zone, occurred within days of each other. We investigate these events by performing waveform analysis, teleseismic *P* wave backprojection, and aftershock relocation. Our results show that the *Mw* 8.2 earthquake ruptured fast (4.1 km/s) and excited frequency-dependent seismic radiation, whereas the *Mw* 7.9 earthquake ruptured slowly (2.5 km/s). Both events lasted ~35 s. The *Mw* 8.2 earthquake initiated in the highly seismogenic, cold core of the slab and likely ruptured into the surrounding warmer materials, whereas the *Mw* 7.9 earthquake likely ruptured through a dissipative process in a previously aseismic region. The contrasts in earthquake kinematics and aftershock productivity argue for a combination of at least two primary mechanisms enabling rupture in the region.

Plain Language Summary Physical mechanisms of deep earthquakes are poorly understood as their ambient environments inhibit brittle slips, which operate shallow earthquake rupture processes. On 19 August 2018, a moment magnitude 8.2 deep earthquake occurred in Tonga, and 18 days later, another moment magnitude 7.9 deep earthquake occurred about 280 km away. These two events are among the largest deep earthquakes that have ever been recorded. We investigate these two events with a variety of seismological techniques and find that these two earthquakes show distinct rupture characteristics and aftershock productivities. The *Mw* 8.2 earthquake ruptured fast, whereas the *Mw* 7.9 earthquake ruptured slowly, despite they both lasted ~35 s. Our observations show that Tonga can host two types of deep earthquakes with diverse and complex source properties, which is rarely observed. More importantly, our observations suggest that multiple physical mechanisms enabled the rupture propagation for the *Mw* 8.2 earthquake, and the *Mw* 8.2 and *Mw* 7.9 earthquake likely ruptured through different physical processes.

1. Introduction

Earthquakes occurring below ~350 km are generally described as deep-focus earthquakes (e.g., Frohlich, 2006; Houston, 2015). At these great depths, the brittle failure processes operating during shallow earthquakes are prohibited by the large ambient stresses (Leith & Sharpe, 1936). The rupture physics responsible for these deep-focus earthquakes is not well understood as they occur infrequently and often have limited observations (e.g., Green & Houston, 1995; Houston, 2015; Wiens, 2001). A few mechanisms have been proposed to explain deep earthquakes, including dehydration embrittlement (Raleigh & Paterson, 1965; Silver et al., 1995), transformational faulting of metastable olivine (Green II & Burnley, 1989; Green & Zhou, 1996; Kirby, 1987; Kirby et al., 1991; Wiens et al., 1993), and thermal shear instability (Hobbs & Ord, 1988; Kanamori et al., 1998; Ogawa, 1987; Wiens & Snider, 2001). The key to distinguish these mechanisms lies in high-resolution seismological observations (Y. Chen et al., 2014; Houston et al., 1998; Persh & Houston, 2004; Poli & Prieto, 2016; Tibi, Bock, & Wiens, 2003; Warren & Silver, 2006; Ye et al., 2013; Zhan et al., 2014). For instance, finite source models of deep earthquakes in Tonga and South American subduction zones have demonstrated two types of distinct rupture characteristics at cold and warm slabs (e.g., Goes & Ritsema,

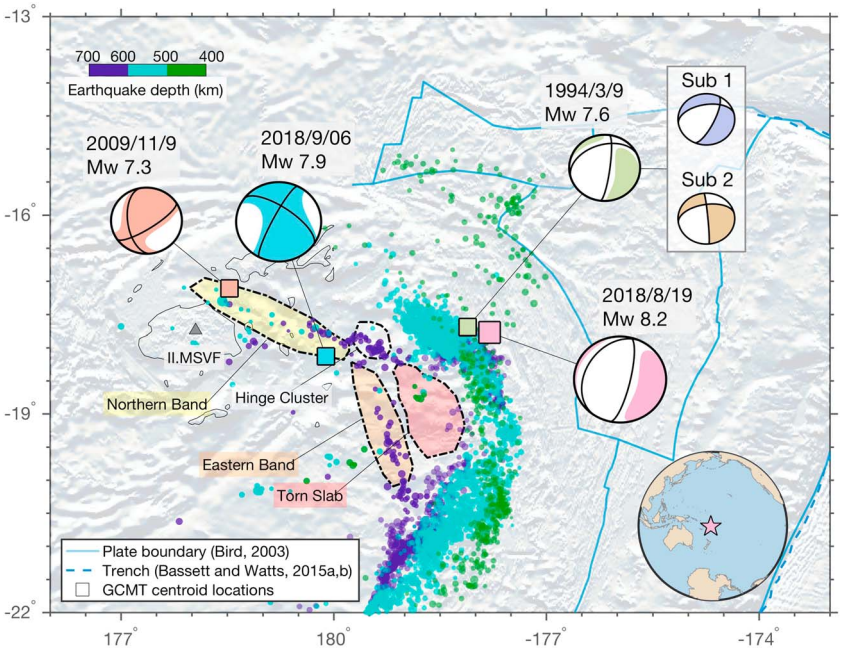

Figure 1. Map view of Tonga-Fiji region. The centroid locations (colored squares) are from the global centroid-moment-tensor (GCMT) catalog (Ekström et al., 2012). The background seismicity is from Cai and Wiens (2016). Focal mechanisms of the two subevents (subevent 1 and subevent2) of the 1994 *Mw* 7.6 Tonga earthquake are from McGuire et al. (1997). The plate boundary and the trench axis are from Bird (2003) and Bassett and Watts (2015a, 2015b). The countered regions are inferred from Cai and Wiens (2016) and W.-P. Chen and Brudzinski (2001). The MSVF station is directly above the 2018 Tonga-Fiji doublet (IRIS/IDA Seismic Network, 1986). The northern band, eastern band, and the Hinge cluster are three seismically active regions, which are related to the last portion of the slab subducted along the fossil Vitiaz trench. A seismic gap (Torn slab) is outlined by a region lacks of seismicity (Cai & Wiens, 2016; W.-P. Chen & Brudzinski, 2001).

1995; Kikuchi & Kanamori, 1994; McGuire et al., 1997; Poli & Prieto, 2014; Tibi, Bock, & Wiens, 2003; Wiens & McGuire, 1995).

Approximately two thirds of the world's deep earthquakes are found in the Tonga subduction zone (Frohlich, 2006). Large deep earthquakes in this region often show fast rupture velocities (≥4 km/s), have high seismic efficiency, and have abundant aftershocks (e.g., McGuire et al., 1997; Warren et al., 2007; Wiens & McGuire, 2000; Zhan, 2017). For instance, the 1994 *Mw* 7.6 Tonga earthquake was recorded by both regional and far-field seismic networks and the combination of high-resolution finite source models with well-located aftershocks clearly showcased these rupture characteristics (McGuire et al., 1997). In addition, the 1994 *Mw* 7.6 Tonga earthquake ruptured beyond the seismically active slab core and likely involved at least three subevents and possibly multiple physical mechanisms (Figure 1; McGuire et al., 1997).

On 19 August 2018, a *Mw* 8.2 deep earthquake occurred ~30 km away from the 1994 *Mw* 7.6 Tonga earthquake (Figure 1). Eighteen days later (6 September 2018), a *Mw* 7.9 deep earthquake occurred ~273 km away from the *Mw* 8.2 earthquake. The *Mw* 8.2 deep earthquake appears to initiate at a depth of ~580 km within a region of dense background seismicity (U.S. Geological Survey, USGS, 2018). The earthquake generated the largest deep earthquake aftershock sequence in total number, including more than 250 aftershocks within 34 days. Its moment tensor solution suggests that the earthquake has a predominant double-couple (DC) normal-faulting focal mechanism (Ekström et al., 2012; USGS, 2018). In contrast, the *Mw* 7.9 earthquake initiated at ~680-km depth in the outboard region beneath the South Fiji Basin with relatively little background seismicity and was followed by a sparse aftershock sequence. It had a strike-slip focal mechanism (Ekström et al., 2012; USGS, 2018) with a large compensated linear vector dipole (CLVD) component (only 34% DC), suggesting a possible complex rupture process involving multiple subevents.

The variety of contrasts in rupture velocity, efficiency, and aftershock productivity between the *Mw* 8.2 and the *Mw* 7.9 Tonga-Fiji deep earthquakes that are only days apart is reminiscent of the global contrast between deep earthquakes in relatively cold and warm slabs (Wiens & McGuire, 1995). Here, we examine the detailed

rupture properties and aftershock distribution of the 2018 Tonga-Fiji deep earthquake sequence with a variety of seismological techniques and examine the implications of this sequence for the rupture mechanisms of deep earthquakes.

2. Data and Methods

2.1. Waveform Analysis

Deep earthquake rupture processes are often complex and have multiple subevents that can be directly identified in their waveforms or source time functions (e.g., Y. Chen & Wen, 2015; Persh & Houston, 2004; Tibi, Bock, & Wiens, 2003). Here we analyze globally recorded seismic records of the *Mw* 8.2 and the *Mw* 7.9 Tonga-Fiji earthquakes. We compare *P* waveforms of the two earthquakes as a function of station azimuth and align the first 55 s of the *P* waves following a similar data processing procedure described in Fan and Shearer (2015; Figure 2).

We downloaded vertical component broadband *P* wave velocity records (BHZ) of the two earthquakes from the Data Management Center of the Incorporated Research Institutions for Seismology. We select all the stations with epicentral distances ranging from 30° to 90° that are registered at the International Federation of Digital Seismograph Networks. First, the instrument responses are removed, and the records are converted to velocity and displacement. A 0.05- to 0.3-Hz fourth-order Butterworth filter is applied to the velocity records for waveform alignment. Records with signal-to-noise ratios less than 2 are removed. The signal-to-noise ratio is defined as the root-mean-square amplitude ratio from time windows 10 s before and 10 s after the theoretical *P* wave arrival obtained from the Preliminary Determination of Epicenters (PDE) Bulletin location and the IASP91 velocity model (Kennett & Engdahl, 1991).

Assuming the first few seconds of the records are radiated from the vicinity of the hypocenter, the waveforms are aligned to minimize the effects of 3-D velocity structures. The alignments are obtained by aligning the filtered velocity records (0.05 to 0.3 Hz) using multichannel cross correlation with a time window from −2 to 8 s relative to the theoretical *P* arrivals (Houser et al., 2008). Cross-correlation polarity flips are allowed during aligning the records to accommodate possible varying radiation patterns at different azimuths. This set of alignments is only used for the subsequent *P* wave polarity and directivity analyses. For the backprojection analysis, new alignments will be obtained with subsets of the data without allowing cross-correlation polarity flips. We then remove records without clear *P* wave onsets by visual inspection. In total, 623 and 464 *P* wavetrains are analyzed for the *Mw* 8.2 and *Mw* 7.9 earthquakes, respectively.

We perform a *P* wave polarity analysis to infer earthquake focal mechanisms. To avoid possible artifacts introduced by filtering, the unfiltered displacement records are analyzed for this part. The waveforms of both earthquakes show great complexities, including *P* wave polarity reversals due to possible multiple subevents with varying focal mechanisms. We first shift the unfiltered displacement records with the obtained alignments, self-normalize the waveforms with their maximum amplitude, and stack the records in 3° wide nonoverlapping azimuthal bins to enhance the coherent phases (Figure 2). To investigate the rupture processes, we then window the *Mw* 8.2 earthquake unfiltered displacement records into 0–8-, 8–22-, and 22–37-s segments and those of the *Mw* 7.9 earthquake into 0–6-, 6–23-, and 23–35-s segments. These time window lengths are guided by the clear *P* wave polarity reversals of the North American stations and the backprojection snapshot results. We identify dominant *P* wave polarities of each time window by visual inspections and then use these polarities to infer possible focal mechanisms through a grid search process (Figure 2). By perturbing the global centroid-moment-tensor (GCMT) project solution (Ekström et al., 2012) fault geometries within 20°, we search for optimal solutions that can fit the observations. The GCMT solution is the preferred solution when it explains the observed polarities. Otherwise, the focal mechanism that explains the most polarity measurements and has the minimum deviation from the GCMT solution is taken as the preferred solution for the given time window. Our approach might be less accurate compared to the multiple-point-moment-tensor inversion. However, the approach is robust and is insensitive to the choice of velocity model. Therefore, we prefer this approach to avoid unknown errors introduced by the complex Tonga-Fiji slab structures (velocity structures). Processing details are in the supporting information.

For large earthquakes, rupture directivity can be estimated from the *P* wave durations (e.g., Fan & Shearer, 2015; Ni et al., 2005; Park & Ishii, 2015). Such analysis is particularly useful for deep earthquakes as the *P* waveforms approximate the moment rate functions (Houston et al., 1998; Tibi, Bock, & Wiens, 2003). We first stack the 0.05- to 0.3-Hz displacement envelope functions by azimuth (3° bin width), which are calculated

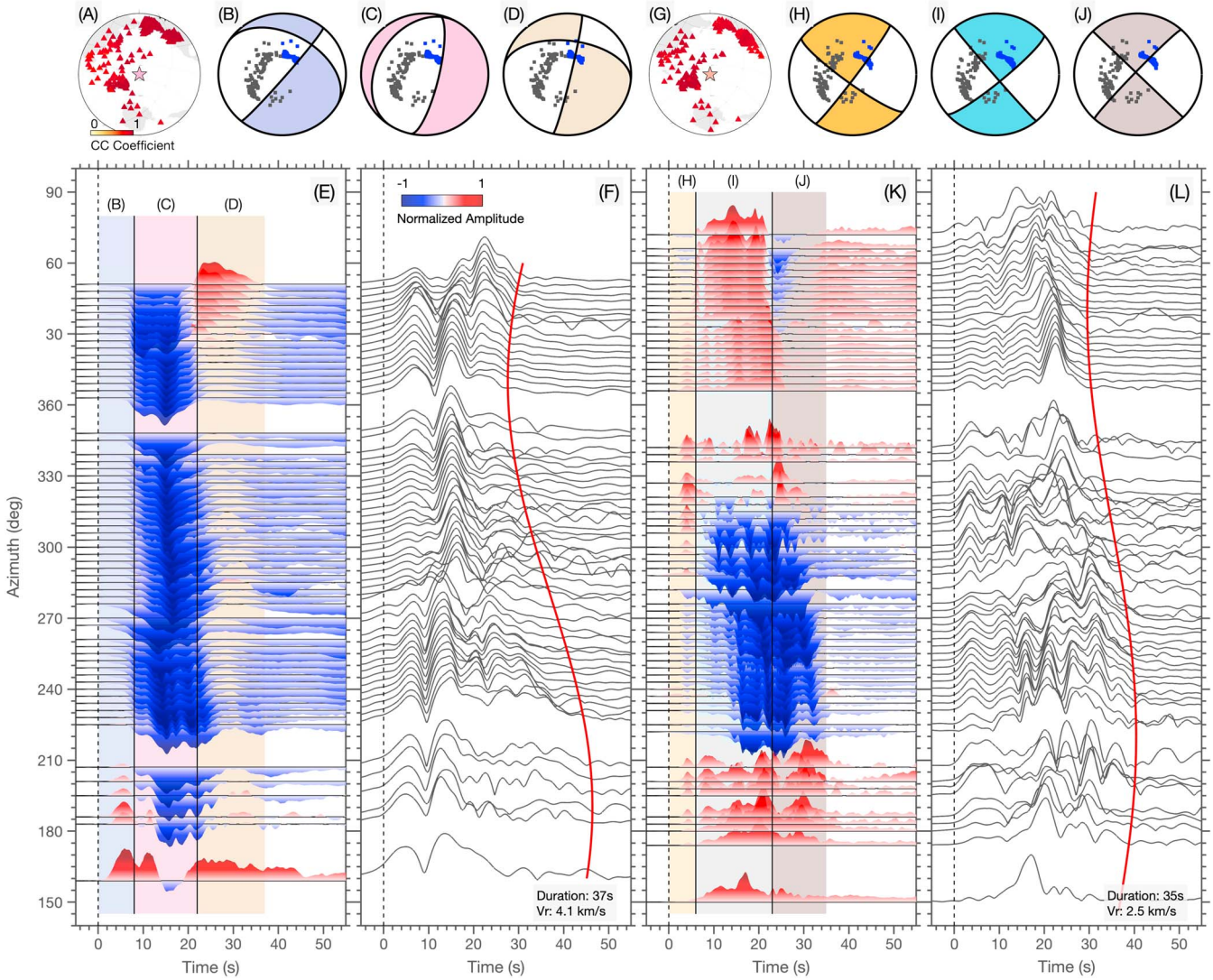

Figure 2. Waveform alignment and subevent focal mechanisms. (a) Stations map of the 2018 *Mw* 8.2 Tonga deep earthquake. The station colors correspond to average cross-correlation coefficients of the first few seconds *P* wave velocity records. CC coefficient legend is shown as insert. (b)–(d) Lower hemisphere focal mechanisms of three subevents of the *Mw* 8.2 event inferred from polarities (0–8, 8–22, and 22–37 s in panel e). The blue dots are North American stations. (e) Aligned self-normalized unfiltered *P* wave displacement records of stations in (a). Positive displacements are shown as red, while negative displacements are shown as blue (color bar legend in panel f). The records are stacked at 3° azimuthal bin to enhance coherent signals. The rectangular color patches show the time windows of the inferred subevents in (b)–(d). (f) Directivity analysis from the envelope functions (3° azimuthal stacking). The *Mw* 8.2 earthquake ruptured toward 10° at 4.1 km/s and lasted 37 s. (g)–(l) are for the *Mw* 7.9 event with similar legends in (a)–(f). The subevents are inferred from polarities of dominant phases of 0–6-, 6–23-, and 23–35-s time windows. In (l), the directivity analysis of the *Mw* 7.9 earthquake shows that the event ruptured toward 40° at 2.5 km/s and lasted 35 s.

with a standard Hilbert transform without smoothing (Figure 2). We then estimate the rupture direction, duration, length, and rupture speed by fitting a cosine curve, assuming that the sources are 1-D unilateral horizontal rupture Haskell models and *P* wave duration variations are caused by the rupture directivity:

$$\delta t_i = T\left(1 - \frac{V_r \cdot \cos(\theta_i - \theta)}{V_i}\right) \quad (1)$$

where T, V_r, and θ are the rupture duration, speed, and direction. The δt_i , θ_i, and V_i are the apparent source duration, azimuth, and apparent velocity for the ith station. For a first-order estimation, we take V_i as 16.76 km/s for all the stations. The source parameters (T, V_r, and θ) are trial-and-error searched by visual inspections of the fit. These approximations do not influence the first-order estimates very much (only three unknowns; Fan & Shearer, 2015). The fitted curves are shown in Figure 2.

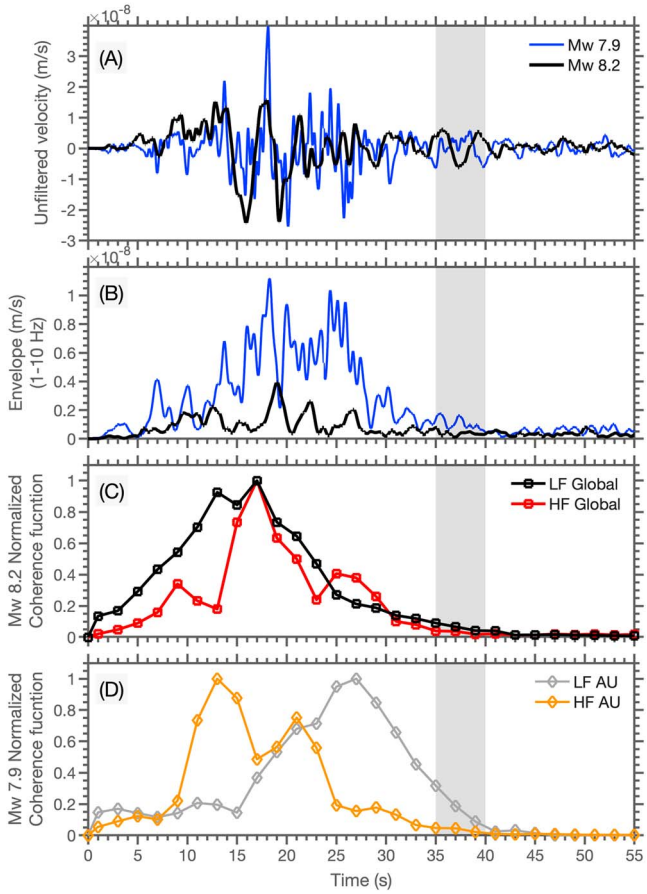

Figure 3. Earthquake durations inferred from the *P* waves of the MSVF station and the linear backprojection peak time functions (coherence functions). (a) Unfiltered *P* wave velocity records of the 2018 *Mw* 8.2 and *Mw* 7.9 Tonga-Fiji deep earthquakes. The gray band shows the range of rupture arresting time. (b) Envelope functions of the two earthquakes. The envelope functions are first calculated from filtered *P* waves at 1–10 Hz and then smoothed by a 0.5-s-long sliding averaging window. (c) Global array peak time functions of the *Mw* 8.2 earthquake at a low-frequency band (LF, 0.05–0.3 Hz) and a high-frequency band (0.3–1 Hz). (d) Australian array (AU) peak time functions of the *Mw* 7.9 earthquake. The legends are similar to (c).

2.2. Backprojection

Backprojection is one of the primary source imaging tools for investigating the rupture propagation of large earthquakes (Fan et al., 2016; Ishii et al., 2005; Kiser & Ishii, 2012; Koper et al., 2011; Meng et al., 2014; Walker et al., 2005; Yagi et al., 2012). Backprojection assumes that the *P* wave records provide relatively undistorted records of seismic radiation, and it takes advantage of source-receiver reciprocity. By stacking the *P* wave records, we can then extract coherent strong signals near earthquake hypocenters as proxies of rupture fronts to map earthquake rupture propagation. In other words, backprojection can serve as a relative location tool that resolves the relative distances between multiple subevents (Fan & Shearer, 2016a). The method is robust, works for high-frequency (HF) waveforms from regional arrays, and is relatively insensitive to complex 3-D velocity structure (e.g., Fan & Shearer, 2017). The method does not require prior assumptions of fault geometry or rupture speed and is particularly useful in studying complex earthquake ruptures and for the detection and localization of multiple subevents. (e.g., Allmann & Shearer, 2007; Fan & Shearer, 2016b; Nissen et al., 2016; Okuwaki et al., 2014; Satriano et al., 2012; Wang et al., 2012).

We perform *P* wave backprojection using the method described in Fan and Shearer (2015). First, *P* wave velocity records that passed the initial quality control in section 2.1 are filtered into two frequency bands, a HF band (0.3–1 Hz) and a low-frequency (LF) band (0.05–0.3 Hz) , to examine the potential frequency dependence of seismic radiation. Second, stations are divided into a few subarrays to avoid imaging artifacts introduced by changing focal mechanisms during the rupture, which may reverse the *P* wave polarity observed in a given direction. The subarrays include the Australian array (AU), the North American array

(NA), and the Global array (stations in East Asia and Australia) for the *Mw* 8.2 earthquake, and the AU and NA arrays for the *Mw* 7.9 earthquake (Figures S1 and S2). Stations of these subarrays share the same polarities during the initial rupture stages (Figures S3 and S4). Third, we align the waveforms of each subarray with multichannel cross correlation at two frequency bands separately (Houser et al., 2008). Here, the cross-correlation time windows are from −2 to 8 s for LF records and from −2 to 3 s for HF records relative to the theoretical *P* arrivals based on the IASP91 model (Kennett & Engdahl, 1991). A maximum 9- and 4-s time shifts are allowed for the two frequency bands, respectively. No cross-correlation polarity flips are allowed during the alignment (Figures S3 and S4). We then grid a set of potential sources around the hypocenters with a 5-km horizontal grid spacing fixed at the hypocentral depths. The potential source grids cover a 300-km by 300-km area for each earthquake, ranging from 19.4°S to 16.9°S and 179.4°W to 176.8°W for the *Mw* 8.2 earthquake and 19.3°S to 16.8S and 178.5°E to 179.9°W for the *Mw* 7.9 earthquake.

Backprojection is then performed with both linear and the *N*th root stacking ($N = 4$). The linear stacking approach can help determine rupture durations and relative radiation strength of different rupture episodes, while *N*th root stacking can improve spatial resolution of backprojection images, albeit at the cost of losing absolute amplitude information (Rost & Thomas, 2002; Xu et al., 2009; Figures 3 and 4). When performing backprojection, the records are self-normalized and inversely scaled by the number of contributing stations within 5°, which can enhance the azimuthal and spatial coverages of the networks. To evaluate the temporal evolution, we obtain a peak power time function (or coherence function) from linear stacking with a nonoverlapping 2-s window that is the maximum backprojected power of the potential sources (location of seismic radiation bursts; Kiser & Ishii, 2013). To evaluate the spatial migration, we compute backprojection snapshots with various stacking windows (Figure 5). The backprojection snapshot time windows are chosen sequentially. For each time window, the length is varied incrementally (1-s step) to achieve a spatially focused image such that only one peak energy loci above 85% of the maximum normalized energy is present. The minimum window length is kept for a high temporal resolution. For each time window, the radiation strength is normalized by the maximum power within that window. The robustness of the resolved snapshots is assessed by Jackknife resampling (Efron & Tibshirani, 1994; Fan & Shearer, 2016a), and we reject snapshots with peak location standard errors greater than 0.5° for either latitude or longitude (~50 km). We do not stack or postprocess the backprojection images to avoid subjective choices.

2.3. Aftershock Relocation

We use the hypocentroidal decomposition relative relocation algorithm (Bergman & Solomon, 1990; Jordan & Sverdrup, 1981) to relocate events in the vicinity of the *Mw* 8.2 earthquake. These events include the *Mw* 8.2 earthquake and its aftershocks (up to 20 September 2018) from the PDE catalog, events reported in the GCMT catalog with *P*, *S*, and *pP* arrivals from the International Seismological Centre (2013) catalog, events recorded by the 2009–2010 Lau Spreading Center Imaging project (Wei et al., 2017), and events recorded by the 1994 Lau Basin Ocean Bottom Seismograph Survey (LABATTS) and the 1993–1995 Southwest Pacific Seismic Experiment (SPASE), which recorded the 1994 *Mw* 7.6 Tonga earthquake and its aftershocks (McGuire et al., 1997; Wiens et al., 1997, 1994). The relocated earthquakes have low depth uncertainties as both regional phase picks from campaign experiments (station locations shown in Figure S5a) and teleseismic arrival times including depth phases are combined to constrain the event locations. As demonstrated in Wei et al. (2017), combining the local data with the International Seismological Centre teleseismic data can significantly improve the depth constraint of events in the region. Depth of events that were only recorded teleseismically can also be greatly improved when being jointly relocated with events that were recorded by both regional and global networks. The relocation is iteratively performed in three steps with uncertainty thresholds of 15, 10, and 8 km. For each iteration, the relocated events that have uncertainties exceeding the threshold are removed before the next iteration. The final earthquake relocations have vertical and lateral uncertainties below 8 km.

3. Results

The *Mw* 8.2 earthquake hypocenter is relocated at 18.23°S/178.01°W/576 km, which is surrounded by its aftershocks. The dense aftershock zone spans ~80 km in depth and ~50 km in length along the NNE direction (Figure S5). These aftershocks are largely contained within the previously seismically active region, delineating the Tonga slab core. In addition, the aftershock zone suggests a nearly vertical fault plane dipping eastward, which agrees with the vertical fault plane (13°/70°/−96°) of the GCMT solution. More geological and geodynamical implications of the relocated background seismicity are beyond the scope of this study

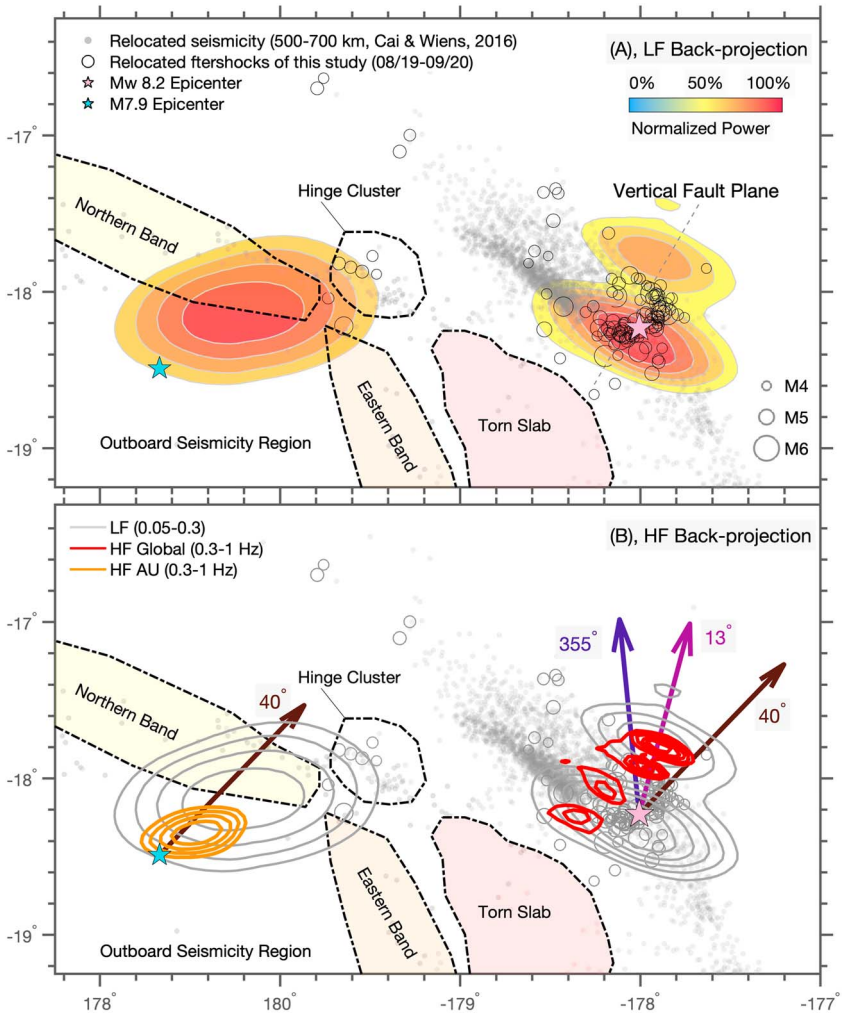

Figure 4. Integrated backprojection images of the two deep earthquakes. (a) Low-frequecy (LF; 0.05–0.3 Hz) integrated backprojection image of the *Mw* 8.2 earthquake from the Global array and that of the *Mw* 7.9 earthquake from the Australian array (AU). The backprojection images show over 50% normalized power for the Global array (*Mw* 8.2 earthquake) and over 60% normalized power for AU array (*Mw* 7.9 earthquake). The *Mw* 8.2 earthquake image has a better spatial resolution due to a larger aperture of the Global array. A set of vertical faults that are subparallel to the thin dashed line direction might have ruptured during the *Mw* 8.2 earthquake. (b) High-frequency (HF; 0.3–1 Hz) integrated backprojection images of the two earthquakes. The backprojection contours show over 50% normalized power for the Global array (*Mw* 8.2 earthquake, both frequencies with 10% increment) and over 60% normalized power for AU array (*Mw* 7.9 earthquake, both frequencies with 10% increment). The colored arrows show strikes of possible subevents. The dark dashed line sketches the fossil Vitiaz and Tonga slab dating from the time of active Vitiaz subduction (Cai & Wiens, 2016). The northern band, the eastern band, and the Hinge cluster separate the outboard seismicity region from the active seismic regions related to the currently subducting Tonga slab. The *Mw* 7.9 earthquake located in a previous aseismic region.

and will be discussed in a separate paper. Directivity analysis suggests the earthquake ruptured toward 10° direction, lasted ~37 s, and propagated with a rupture speed of 4.1 km/s, which lead to a rupture length of ~152 km (Figure 2f). To confirm that our estimate of the rupture duration is not biased by a strong vertical component of directivity, we examine the *P* wave recorded at a nearby MSVF station (Figure 1), at which the *P* waves have an opposite (upward) take-off direction than the teleseismic arrays (Figures 3a and 3b). Its unfiltered velocity record and envelope function (1–10 Hz) show that the earthquake arrested before 40 s after its initiation (Figures 3a and 3b) similar to the estimate obtained from the directivity analysis. The ~37-s duration is also confirmed by the linear backprojection peak time functions in both HF and LF frequency bands (Figure 3c).

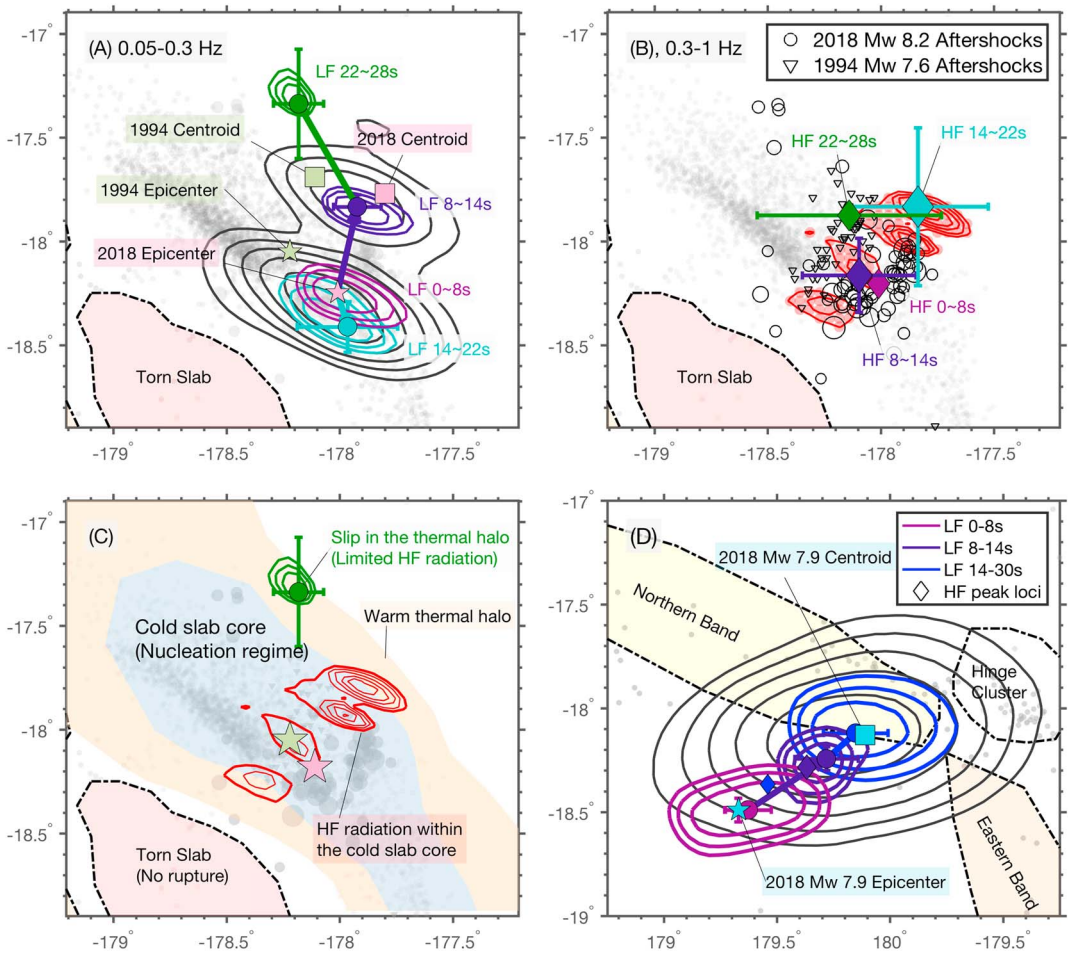

Figure 5. Backprojection snapshots. (a) Low-frequency (LF) snapshots for the *Mw* 8.2 earthquake. (b) High-frequency (HF) snapshots for the *Mw* 8.2 earthquake. (c) One conceptual model explaining the observed seismic radiation patterns of the *Mw* 8.2 earthquake. (d) Snapshots for the *Mw* 7.9 earthquake of both frequency bands. The location error bars are derived from station Jackknife resampling. The stars show the epicenter locations, and the squares show the global centroid-moment-tensor centroid locations. The colored circles/diamonds show the peak power loci of LF/HF backprojection snapshots. The integrated backprojection contours share similar legends as those in Figure 4. The snapshot contours show over 85% normalized power of each time window with 5% increment for both earthquakes.

The Global array *N*th root LF backprojection results show that the *Mw* 8.2 earthquake ruptured northeastward for about 1° (110 km) in length (Figure 4a). The first 22 s of LF radiation is confined within ~50 km where most of the aftershocks occurred, whereas the 22- to 28-s LF radiation occurred outside of the aftershock zone and is located ~102 km away from the epicenter (Figure 5a). These LF backprojection snapshots suggest a northward rupture propagation at an average speed of ~4 km/s for the *Mw* 8.2 earthquake. The integrated HF backprojection results from multiple subarrays independently show that the majority of the HF radiation was released within the aftershock zone (Figures 4b and S6). The Global array HF backprojection snapshots show that the peak loci are compactly confined within a linear band, which is different from the LF backprojection snapshots (Figures 5a and 5b). Neither LF nor HF backprojection images show a significant southward rupture propagation as little seismic radiation is located south of the hypocenter, which is consistent with the aftershock distribution (Figures 4 and 5).

The *Mw* 7.9 earthquake likely occurred within a detached slab segment west of the main Tonga slab. The earthquake has few aftershocks near its hypocenter (USGS, 2018). Directivity analysis shows that the earthquake ruptured toward the 40° direction (Figure 2l), which agrees well with the 207°/77°/146° (strike/dip/rake) nodal plane reported by GCMT (Ekström et al., 2012). The earthquake ruptured ~88 km in length, lasted ~35 s, and propagated with an average rupture speed of 2.5 km/s (Figure 2l). We also verify the rupture duration estimate by examining the *P* wave duration of the MSVF station as well as the linear back-

projection peak time functions in both the HF and LF frequency bands. The observations consistently show that the earthquake lasted ~35 s (Figure 3). The *N*th root integrated backprojection results of both frequency bands show that the majority of the seismic radiation was released northeast of the hypocenter (Figure 4). However, the coherence functions show that the majority LF energy release occurred much later than that of HF radiation (Figure 3). The LF backprojection snapshots agree well with the directivity analysis, locating the most energetic episode (between 14 and 30 s) as occurring ~70 km away from the *Mw* 7.9 earthquake epicenter. This episode collocates with the GCMT centroid location. The HF backprojection snapshots show a similar but more compact rupture pattern (Figure 5d).

Both the *Mw* 8.2 and the *Mw* 7.9 earthquakes ruptured multiple faults as shown by the changes in focal mechanism during the rupture (Figure 2). Focal mechanisms inferred from *P* wave displacement polarities suggest that the *Mw* 8.2 earthquake initiated on a fault plane striking at 40° (40°/85°/−60° for strike/dip/rake, Figure 2b), evolved into a mechanism similar to the GCMT solution 13° (13°/70°/−96°; Figure 2c), and arrested on a fault plane striking at 13° (13°/85°/−50°, Figure 2d). For the *Mw* 8.2 earthquake, the *P* wave polarities remained negative during the whole rupture process for stations in Australia and East Asia, while the polarities reversed from positive to negative for stations in Antarctica around ~8 s and reversed from negative to positive for stations in North America around ~22 s. Thus, the strike of the *Mw* 8.2 earthquake rotated by 27° or sequentially activated faults of these different orientations. Focal mechanism variations are also observed during the *Mw* 7.9 earthquake. This event initiated on a fault with strike/dip/rake as 36°/85°/167° during the first 6 s, ruptured a second fault striking at 50° (50°/78°/178°), and arrested on a fault striking at 223° (223°/86°/155°). The last subevent focal mechanism is similar to one of the nodal planes reported by the GCMT solution (207°/77°/149°). The focal mechanisms suggest that there were a ~20° dip change from dipping toward NW to toward SE and a ~15° strike rotation occurred during the *Mw* 7.9 earthquake rupture. This series of variations is particularly required by the North American stations as they are situated in the rupture propagation direction.

4. Discussions

Deep earthquakes have relatively clean *P* waves, which are free from contamination by depth phases or water reverberations (e.g., Fan & Shearer, 2018; Tibi, Bock, & Wiens, 2003), making their backprojection results generally robust. To assess the backprojection image uncertainties, we performed seven different types of tests, including imaging major rupture features with multiple subarrays (Figures 4 and S6), evaluating the Global array response function (20-km radius of the backprojection image, Figure S7a), backprojection with *pP* records (Figure S7b), imaging a nearby *Mw* 5.7 aftershock (28 August 2018) with both its self-alignment and using the mainshock alignment derived from the LF band of the Global array (40 km radius of the backprojection image, Figures S7c and S7d), quantitively evaluating snapshot location uncertainties with Jackknife resampling (Figure 5), and validating the *Mw* 8.2 event's 22- to 28-s LF snapshot location with arrays at various azimuths (Figure S8). Of particular importance for our physical interpretations discussed below, the 22- to 28-s LF episode produced clear, well-isolated phases across the whole azimuthal range. These arrivals are particularly strong and have positive polarities at stations from North America, which were not used for imaging this subevent (Figure S8). The combination of observations from different arrays assures the confidence of the well-resolved relative location of the 22- to 28-s LF subevent. Additionally, we used the Hi-net stations in Japan (e.g., Obara et al., 2005; Okada et al., 2004) to image the rupture processes of these two events at 0.5–5 Hz following the same procedure (Figures 3, 4, and S1–S4), which verified the HF backprojection results obtained with other arrays. Collectively, these tests indicate that our backprojection results are well resolved and have low uncertainties. Further details are in the supporting information.

There are many similarities between the 2018 *Mw* 8.2 and 1994 *Mw* 7.6 Tonga-Fiji earthquakes. Both events produced many aftershocks that align with their steeply dipping NNE striking focal planes in an orientation that is nearly perpendicular to the SE striking Tonga slab. Additionally, both ruptures initiated in the interior of the highly seismic, near vertical slab close to its SW edge (McGuire et al., 1997; Wiens et al., 1994) and then ruptured predominately northward at a rupture speed of ~4 km/s while involving at least three subevents with varying focal mechanisms (McGuire et al., 1997). The 1994 *Mw* 7.6 earthquake terminated in a region about 200 °C warmer than the temperature delimiting the normally seismogenic portion of the slab, in a thermal "halo" where ruptures appear to be able to propagate but earthquake nucleation is inhibited (McGuire et al., 1997). Similarly, the last LF subevent (22–28 s) of the 2018 Tonga *Mw* 8.2 earthquake was also concentrated in the thermal halo region, where few aftershocks occurred (Figure 5). The lack of

significant HF radiation at the location of the 22- to 28-s LF episode suggests that the last subevent of the *Mw* 8.2 earthquake was relatively deficient in HF radiation. Combining the observations from the two earthquakes, the warmer halo region has difficulty nucleating rupture, but large ruptures regularly propagate into this region perhaps under a different physical mechanism that produces relatively deficient HF radiation compared to the nucleation mechanism in the colder core of the slab.

In addition to the resolved along-strike rupture, there must have been rupture propagation along the dip direction. The aftershock distribution suggests a ~80-km along-dip rupture extent (Figure S5; USGS, 2018). However, durations inferred from upgoing and downgoing *P* waves are about the same (Figures 2 and 3), suggesting that the *Mw* 8.2 earthquake ruptured bilaterally along dip and the updip and downdip rupture extents were relatively symmetric. The varying focal mechanisms of the multiple subevents of both the 2018 *Mw* 8.2 and the 1994 *Mw* 7.6 earthquakes confirm that the local stress field is highly heterogenous (Figures 2 and 4; Warren et al., 2007).

Our estimate of the rupture length of the 2018 Tonga-Fiji *Mw* 8.2 earthquake ranges from ~152 km (from the directivity analysis) to ~102 km (from the backprojection). This discrepancy likely results from the the simplified 1-D line source model and the 14- to 22-s radiation episode (Figure 5). The 1-D rupture model assumes the directivity effects (*P* wave duration variations) result from a continuously propagating rupture front. However, the 14- to 22-s LF radiation episode is close to the epicenter. This "pausing" episode lasted for about 8 s, which would lead to a ~33-km rupture length estimate. In addition, the imaged 22- to 28-s LF episode may not be the arresting point as backprojection may lose its resolution due to the increase of the noise level and the small amplitude of late signals. Therefore, the *Mw* 8.2 earthquake could have extended further than ~102 km. In Figure 3b, the envelope function of the MSVF station (1–10 Hz) shows a shorter rupture duration (~30 s) of the *Mw* 8.2 earthquake than that estimated from the backprojection and directivity analysis (~35 s). This is likely because the last episode ruptured in the thermal halo region was HF deficient. As shown in Figure 3a, the unfiltered velocity seismograph of the MSVF station has a prominent phase from 35 to 40 s, suggesting the event continued rupturing till ~35 s. Backprojection snapshots of LF radiation after 28 s have large spatial uncertainties leaving the locations less well determined.

The 2018 Tonga-Fiji *Mw* 7.9 earthquake has distinctive rupture characteristics compared to the 2018 *Mw* 8.2 earthquake. The earthquake occurred in a relatively aseismic region west of the main Tonga slab and shows a depth difference between the hypocenter (670 km, PDE) and centroid (~690 km, GCMT solution). The moment of the *Mw* 7.9 earthquake is 3 times smaller than that of the *Mw* 8.2 earthquake, but the durations of the two events are comparable (Figures 2 and 3). The 2018 *Mw* 7.9 earthquake ruptured significantly slower (2.5 km/s) compared to the 2018 *Mw* 8.2 earthquake (4.1 km/s) or the nearby 2009 *Mw* 7.3 Fiji earthquake (~4.6 km/s, Figure 1; Cai & Wiens, 2016). Furthermore, the 2018 *Mw* 7.9 earthquake only generated a few aftershocks that are not located near the hypocenter (Figure 4; USGS, 2018). These aftershocks were likely dynamically triggered along a diffuse line of seismicity that may represent a slab fragment from the relict Vitiaz Trench (Cai & Wiens, 2016). These characteristics share many similarities with isolated large deep earthquakes in the South American subduction zone, for example, the 1994 *Mw* 8.2 Bolivia earthquake, which appear to represent a separate class of deep earthquakes comparing to typical Tonga deep earthquakes (Kikuchi & Kanamori, 1994; Tibi, Bock, & Wiens, 2003; Wiens & McGuire, 1995). The observations suggest that the 2018 Fiji *Mw* 7.9 earthquake propagated with a more dissipative process. Such a rupture process releases most of the earthquake energy through rupture melting instead of radiating as seismic waves (Kanamori et al., 1998). The ambient environment around the hosting faults is likely too warm to initiate a high rate of background seismicity, but it can sustain large displacements once rupture is initiated (Tibi, Bock, & Wiens, 2003; Zhan, 2017). The USGS *W*-phase focal mechanism has a significantly large CLVD component (only 34% DC), while the *Mw* 8.2 event only had a 11% CLVD component despite that both earthquakes involved at least three subevents (Duputel et al., 2012; Hayes et al., 2011). The large CLVD component also seems abnormal when comparing to that of the 2002 *Mw* 7.7 Tonga deep earthquake, which occurred in an aseismic region nearby with an only 15% CLVD component. The dissipative rupture process of the *Mw* 7.9 Fiji earthquake might be part of the cause of the large CLVD component. However, further investigations are needed to unravel the nature of the large CLVD component of this earthquake.

The 2018 *Mw* 8.2 and *Mw* 7.9 Tonga-Fiji deep earthquakes occurred sequentially within 18 days and 270 km apart of one another and hence are likely related. The absence of background seismicity near the hypocenter of the *Mw* 7.9 event renders a chance occurrence unrelated to the earlier *Mw* 8.2 extremely unlikely.

As deep earthquakes are known to be susceptible to triggering (Myers et al., 1995; Tibi, Wiens, & Inoue, 2003), it seems likely that the *Mw* 7.9 earthquake was triggered by the *Mw* 8.2 earthquake. To test possible influences from static triggering, we calculate the local Coulomb stress changes with the vertical fault plane USGS finite-fault model of the *Mw* 8.2 earthquake (e.g., Hayes, 2011; Lin & Stein, 2004; Toda et al., 2005). We compute Coulomb stress changes induced on the 207°/77°/149° fault plane of the *Mw* 7.9 event (GCMT solution) at 670-km depth with a shear modulus of 1.16E11 Pa, a Poisson's ratio of 0.24, and an apparent friction coefficient of 0.7, which are suggested in Cai and Wiens (2016). Stress contours of Figure S9 show areas with stress perturbations exceeding 10 kPa, and the *Mw* 7.9 earthquake is located outside of these stress contours. This suggests that the static Coulomb stress induced by the *Mw* 8.2 event alone is not sufficient to drive the failure of the *Mw* 7.9 earthquake (Figure S9). Dynamic triggering of deep earthquakes has been reported in nearby regions (Cai & Wiens, 2016; Tibi, Wiens, & Inoue, 2003). Such correlated seismic activities between fault systems have also been observed for other large deep earthquake sequences (Tibi, Wiens, & Inoue, 2003). Given the complex stress field of the Tonga subduction zone at these depths, it is possible that the *Mw* 7.9 event was dynamically triggered by the *Mw* 8.2 earthquake. However, for shallow earthquakes, dynamic triggering usually coincides with large-amplitude seismic wave arrivals or occurs soon after the seismic wave passage, usually within a few days (e.g., Peng et al., 2010). The 18-day delay time is unusually long and suggests possible differences with previously observed deep earthquake dynamic triggering, in which triggering is limited to a few hours or days (Cai & Wiens, 2016; Tibi, Wiens, & Inoue, 2003). The dynamic triggering of the second large 2018 Tonga-Fiji event may have involved a more complex aseismic cascading processes preceding the rupture initiation, though data are not available to test this hypothesis.

The 2018 Tonga-Fiji deep earthquakes show similar rupture characteristics to the August 2002 Tonga deep earthquake sequence (Tibi, Wiens, & Inoue, 2003). The first earthquake in each sequence, the 2002 *Mw* 7.6 Tonga earthquake and the 2018 *Mw* 8.2 earthquake, involves multiple episodes of moment release and demonstrates clear directivity effects (Tibi, Wiens, & Inoue, 2003). The 2002 *Mw* 7.7, the second event of the 2002 earthquake sequence, showed no evidence of rupture directivity, suggesting a very slow rupture speed (Tibi, Wiens, & Inoue, 2003), which shares resemblance with the 2018 *Mw* 7.9 Fiji earthquake. Both deep earthquake sequences involve the second earthquake being dynamically triggered in aseismic regions, whereas the first earthquake was situated in seismically active regions, which are likely in slab cores. These similarities suggest that the Tonga subduction zone might be prone to hosting large deep earthquake doublets.

The 2018 *Mw* 8.2 Tonga earthquake show similarities with the largest deep earthquake on record, the 2013 *Mw* 8.3 Sea of Okhotsk earthquake (e.g., Park & Ishii, 2015; Zhan et al., 2014). For instance, the 2013 *Mw* 8.3 Sea of Okhotsk earthquake also ruptured through a complex process, involving multiple subevents with different focal mechanisms (Y. Chen et al., 2014), propagating with a fast rupture speed (Wei et al., 2013) and a possible frequency-dependent seismic radiation (Meng et al., 2014). Similarities between the 2018 *Mw* 8.2 Tonga earthquake and the 2013 *Mw* 8.3 Sea of Okhotsk earthquake likely reflect that both the Tonga and Kuril subduction zones are relatively cold thermal state and that the earthquake rupture processes are controlled by their local physical environments (Wiens & Gilbert, 1996).

Tonga and South America host large deep earthquakes that represent two end-member rupture scenarios (Wiens & McGuire, 1995). The variation is considered an expression of the local thermal structures of these subducted slabs. In the Tonga subduction zone, large deep earthquakes often initiate in the cold core of the slab, which leads to fast rupture, high seismic efficiency, large rupture extent (regular stress drops), and high aftershock productivity (e.g., Green & Houston, 1995; Houston, 2015; Wiens, 2001). In the South American subduction zone, large deep events are often quite isolated with few aftershocks, have low seismic efficiency, rupture limited spatial extent (high stress drops), and propagate slowly during the coseismic rupture (e.g., Green & Houston, 1995; Houston, 2015; Wiens, 2001). One exception in the South American subduction zone is the 1991 *Mw* 7.2 Argentina earthquake, which shows rupture characteristics that are more akin to those of typical large deep earthquakes in Tonga (Tibi, Bock, & Wiens, 2003). This shows that the South America subduction zone can host both types of deep earthquakes and that local small-scale structure is critical to modulating the large deep earthquake rupture propagation. Here, rupture processes of the 2018 Tonga-Fiji deep earthquake doublet suggests that the Tonga subduction zone can also host both types of deep earthquakes within a ~300-km separation. Based on the source imaging and aftershock distributions, the *Mw* 8.2 earthquake is likely to have a stress drop of 2.6 MPa (rectangular fault model, length 100 km

by width 80 km), which is comparable to shallow earthquakes. If the *Mw* 7.9 earthquake had as high a stress drop (~100 MPa) as that of the 1994 *Mw* 8.2 Bolivia earthquake (Kanamori et al., 1998; Kikuchi & Kanamori, 1994), the rupture width of the event would be about only 8.5 km along dip given the rupture length is about 80 km (Figure 2). However, there is no aftershock distribution to confirm the rupture width, and backprojection cannot resolve the depth extent, leaving the estimate to be verified by future studies.

The similar rupture propagation patterns between the 2018 Tonga *Mw* 8.2 earthquake and the 1994 Tonga *Mw* 7.6 earthquake suggest that they were likely governed by the same physical mechanisms. The rupture initiated in the cold slab core through either transformational faulting or thermal runaway and then propagated into a hotter material regime, where sliding was sustained by ductile faulting or a shear instability mechanism (Hobbs & Ord, 1988; McGuire et al., 1997; Ogawa, 1987). The aftershock distributions of both the 2018 *Mw* 8.2 and the 1994 *Mw* 7.6 Tonga earthquakes show that they occurred on two different faults that are parallel to each other. Therefore, faulting through metastable olivine transformation may be responsible for the rupture initiation, because two parallel en echelon faults may have hosted these two events respectively (e.g., W.-P. Chen, 1995), and both ruptures initiated in the cold slab core where metastable olivine is expected. On the other hand, the region near the 2018 Fiji *Mw* 7.9 earthquake is unlikely to have a sufficient amount of metastable olivine to accommodate the whole rupture process as shown by the paucity of aftershocks and the lack of background seismicity. Therefore, the *Mw* 7.9 earthquake may have ruptured through one or more thermal shear instability mechanisms. The nucleation mechanism of the *Mw* 7.9 earthquake is unclear as the structure of the source region, and its relationship to any slab fragments is largely unknown.

5. Conclusion

The 2018 *Mw* 8.2 and *Mw* 7.9 Tonga-Fiji earthquake doublet provides an excellent opportunity to investigate deep earthquake rupture mechanisms. The *Mw* 8.2 earthquake ruptured one or more subparallel vertical fault planes, lasted ~37 s, had an average rupture speed of 4.1 km/s, and generated more than 250 aftershocks spanning a ~50-km by ~100-km area. The earthquake initiated in the cold slab core, propagated toward the northeast, and arrested in the warmer thermal halo regime. Fault slip in the warmer material produced clear LF phases that can be identified at all azimuths while producing little HF seismic radiation. The *Mw* 7.9 earthquake ruptured toward the northeast (40°), lasted ~35 s, had an average rupture speed of 2.5 km/s, and experienced at least two strike rotations. The earthquake occurred in the Tonga-Fiji outboard region and generated very few aftershocks. The *Mw* 8.2 earthquake resembles rupture characteristics of other large deep earthquakes in the region. In particular, the *Mw* 8.2 earthquake rupture propagation was highly similar to that of the 1994 *Mw* 7.6 Tonga earthquake. The rupture characteristics of the *Mw* 7.9 earthquake are less commonly observed in Tonga but are more similar to those of large deep earthquakes in South American. Our observations show that Tonga can host two types of earthquakes with diverse and complex source properties. Our observations suggest the *Mw* 8.2 earthquake was likely initiated by transformational faulting and ruptured into aseismic regions by ductile faulting or shear instability. We suggest that the *Mw* 7.9 earthquake rupture propagation was unlikely to have occurred through transformational faulting but more likely by way of one or more thermal shear instability mechanisms.

Acknowledgments
We thank the Editor Gavin Hayes and two anonymous reviewers for their helpful comments that improved the quality of the manuscript. The seismic data were provided by Data Management Center (DMC) of the Incorporated Research Institutions for Seismology (IRIS). The facilities of IRIS Data Services, and specifically the IRIS Data Management Center, were used for access to waveforms, related metadata, and/or derived products used in this study. IRIS Data Services are funded through the Seismological Facilities for the Advancement of Geoscience and EarthScope (SAGE) Proposal of the National Science Foundation under Cooperative Agreement EAR-1261681. W. F. acknowledges supports from the Postdoctoral Scholar Program at the Woods Hole Oceanographic Institution, with funding provided by the Weston Howland Postdoctoral Scholarship. S. S. W. and D. T. are supported by the MSU Geological Sciences Endowment.

References

Allmann, B. P., & Shearer, P. M. (2007). A high-frequency secondary event during the 2004 Parkfield earthquake. *Science*, *318*(5854), 1279–1283.

Bassett, D., & Watts, A. B. (2015a). Gravity anomalies, crustal structure, and seismicity at subduction zones: 1. Seafloor roughness and subducting relief. *Geochemistry, Geophysics, Geosystems*, *16*, 1508–1540. https://doi.org/10.1002/2014GC005684

Bassett, D., & Watts, A. B. (2015b). Gravity anomalies, crustal structure, and seismicity at subduction zones: 2. Interrelationships between fore-arc structure and seismogenic behavior. *Geochemistry, Geophysics, Geosystems*, *16*, 1541–1576. https://doi.org/10.1002/2014GC005685

Bergman, E. A., & Solomon, S. C. (1990). Earthquake swarms on the Mid-Atlantic Ridge: Products of magmatism or extensional tectonics? *Journal of Geophysical Research*, *95*(B4), 4943–4965.

Bird, P. (2003). An updated digital model of plate boundaries. *Geochemistry, Geophysics, Geosystems*, *4*(3), 1027. https://doi.org/10.1029/2001GC000252

Cai, C., & Wiens, D. A. (2016). Dynamic triggering of deep earthquakes within a fossil slab. *Geophysical Research Letters*, *43*, 9492–9499. https://doi.org/10.1002/2016GL070347

Chen, W.-P. (1995). En echelon ruptures during the great Bolivian earthquake of 1994. *Geophysical Research Letters*, *22*(16), 2261–2264.

Chen, W.-P., & Brudzinski, M. R. (2001). Evidence for a large-scale remnant of subducted lithosphere beneath Fiji. *Science*, *292*(5526), 2475–2479.

Chen, Y., & Wen, L. (2015). Global large deep-focus earthquakes: Source process and cascading failure of shear instability as a unified physical mechanism. *Earth and Planetary Science Letters*, *423*, 134–144.
Chen, Y., Wen, L., & Ji, C. (2014). A cascading failure during the 24 May 2013 great Okhotsk deep earthquake. *Journal of Geophysical Research: Solid Earth*, *119*, 3035–3049. https://doi.org/10.1002/2013JB010926
Duputel, Z., Rivera, L., Kanamori, H., & Hayes, G. (2012). W phase source inversion for moderate to large earthquakes (1990–2010). *Geophysical Journal International*, *189*(2), 1125–1147. https://doi.org/10.1111/j.1365-246X.2012.05419.x
Efron, B., & Tibshirani, R. J. (1994). *An introduction to the bootstrap*. Boca Raton, FL: CRC press.
Ekström, G., Nettles, M., & Dziewoński, A. (2012). The global CMT project 2004–2010: Centroid-moment tensors for 13,017 earthquakes. *Physics of the Earth and Planetary Interiors*, *200–201*(0), 1–9. https://doi.org/10.1016/j.pepi.2012.04.002
Fan, W., & Shearer, P. (2015). Detailed rupture imaging of the 25 April 2015 Nepal earthquake using teleseismic *P* waves. *Geophysical Research Letters*, *42*, 5744–5752. https://doi.org/10.1002/2015GL064587
Fan, W., & Shearer, P. M. (2016a). Local near instantaneously dynamically triggered aftershocks of large earthquakes. *Science*, *353*(6304), 1133–1136. https://doi.org/10.1126/science.aag0013
Fan, W., & Shearer, P. M. (2016b). Fault interactions and triggering during the 10 January 2012 *Mw* 7.2 Sumatra earthquake. *Geophysical Research Letters*, *43*, 1934–1942. https://doi.org/10.1002/2016GL067785
Fan, W., & Shearer, P. M. (2017). Investigation of back-projection uncertainties with M6 earthquakes. *Journal of Geophysical Research: Solid Earth*, *122*, 7966–7986. https://doi.org/10.1002/2017JB014495
Fan, W., & Shearer, P. M. (2018). Coherent seismic arrivals in the *P* wave coda of the 2012 *Mw* 7.2 Sumatra earthquake: Water reverberations or an early aftershock? *Journal of Geophysical Research: Solid Earth*, *123*, 3147–3159. https://doi.org/10.1002/2018JB015573
Fan, W., Shearer, P. M., Ji, C., & Bassett, D. (2016). Multiple branching rupture of the 2009 Tonga-Samoa earthquake. *Journal of Geophysical Research: Solid Earth*, *121*, 5809–5827. https://doi.org/10.1002/2016JB012945
Frohlich, C. (2006). *Deep earthquakes*. Cambridge: Cambridge University Press.
Goes, S., & Ritsema, J. (1995). A broadband *P* wave analysis of the large deep Fiji island and Bolivia earthquakes of 1994. *Geophysical Research Letters*, *22*(16), 2249–2252.
Green, H. W., & Houston, H. (1995). The mechanics of deep earthquakes. *Annual Review of Earth and Planetary Sciences*, *23*(1), 169–213.
Green Ii, H., & Burnley, P. (1989). A new self-organizing mechanism for deep-focus earthquakes. *Nature*, *341*(6244), 733–737.
Green, H. W. II, & Zhou, Y. (1996). Transformation-induced faulting requires an exothermic reaction and explains the cessation of earthquakes at the base of the mantle transition zone. *Tectonophysics*, *256*(1-4), 39–56.
Hayes, G. P. (2011). Rapid source characterization of the 2011 *Mw* 9.0 off the Pacific coast of Tohoku earthquake. *Earth, Planets, Space*, *63*(7), 529–534. https://doi.org/10.5047/eps.2011.05.012
Hayes, G. P., Earle, P. S., Benz, H. M., Wald, D. J., Briggs, R. W., & the USGS/NEIC Earthquake Response Team (2011). 88 hours: The U.S. Geological Survey National Earthquake Information Center response to the 11 March 2011 *Mw* 9.0 Tohoku earthquake. *Seismological Research Letters*, *82*(4), 481–493. https://doi.org/10.1785/gssrl.82.4.481
Hobbs, B. E., & Ord, A. (1988). Plastic instabilities: Implications for the origin of intermediate and deep focus earthquakes. *Journal of Geophysical Research*, *93*(B9), 10,521–10,540.
Houser, C., Masters, G., Shearer, P., & Laske, G. (2008). Shear and compressional velocity models of the mantle from cluster analysis of long-period waveforms. *Geophysical Journal International*, *174*(1), 195–212. https://doi.org/10.1111/j.1365-246X.2008.03763.x
Houston, H. (2015). 4.13—deep earthquakes. In G. Schubert (Ed.), *Treatise on geophysics* (2nd ed., pp. 329–354). Oxford: Elsevier. https://doi.org/10.1016/B978-0-444-53802-4.00079-8
Houston, H., Benz, H. M., & Vidale, J. E. (1998). Time functions of deep earthquakes from broadband and short-period stacks. *Journal of Geophysical Research*, *103*(B12), 29,895–29,913.
IRIS/IDA Seismic Network (1986). Scripps Institution of Oceanography (1986): IRIS/IDA seismic network. International Federation of Digital Seismograph Networks. https://doi.org/10.7914/sn/ii
International Seismological Centre (2013). *On-line bulletin*. United Kingdom: Int. Seis. Cent., Thatcham. Retrieved from http://www.isc.ac.uk
Ishii, M., Shearer, P. M., Houston, H., & Vidale, J. E. (2005). Extent, duration and speed of the 2004 Sumatra-Andaman earthquake imaged by the Hi-net array. *Nature*, *435*(7044), 933–936.
Jordan, T. H., & Sverdrup, K. A. (1981). Teleseismic location techniques and their application to earthquake clusters in the south-central Pacific. *Bulletin of the Seismological Society of America*, *71*(4), 1105–1130.
Kanamori, H., Anderson, D. L., & Heaton, T. H. (1998). Frictional melting during the rupture of the 1994 Bolivian earthquake. *Science*, *279*(5352), 839–842.
Kennett, B. L. N., & Engdahl, E. R. (1991). Traveltimes for global earthquake location and phase identification. *Geophysical Journal International*, *105*(2), 429–465. https://doi.org/10.1111/j.1365-246X.1991.tb06724.x
Kikuchi, M., & Kanamori, H. (1994). The mechanism of the deep Bolivia earthquake of June 9, 1994. *Geophysical Research Letters*, *21*(22), 2341–2344.
Kirby, S. H. (1987). Localized polymorphic phase transformations in high-pressure faults and applications to the physical mechanism of deep earthquakes. *Journal of Geophysical Research*, *92*(B13), 13,789–13,800.
Kirby, S. H., Durham, W. B., & Stern, L. A. (1991). Mantle phase changes and deep-earthquake faulting in subducting lithosphere. *Science*, *252*(5003), 216–225.
Kiser, E., & Ishii, M. (2012). Combining seismic arrays to image the high-frequency characteristics of large earthquakes. *Geophysical Journal International*, *188*(3), 1117–1128. https://doi.org/10.1111/j.1365-246X.2011.05299.x
Kiser, E., & Ishii, M. (2013). Hidden aftershocks of the 2011 *Mw* 9.0 Tohoku, Japan earthquake imaged with the backprojection method. *Journal of Geophysical Research: Solid Earth*, *118*, 5564–5576. https://doi.org/10.1002/2013JB010158
Koper, K. D., Lay, A. H. T., Ammon, C., & Kanamori, H. (2011). Frequency-dependent rupture process of the 2011 M 9.0 Tohoku earthquake: Comparison of short-period *P* wave backprojection images and broadband seismic rupture models. *Earth Planets and Space*, *63*(7), 599.
Leith, A., & Sharpe, J. (1936). Deep-focus earthquakes and their geological significance. *The Journal of Geology*, *44*(8), 877–917.
Lin, J., & Stein, R. S. (2004). Stress triggering in thrust and subduction earthquakes and stress interaction between the southern San Andreas and nearby thrust and strike-slip faults. *Journal of Geophysical Research*, *109*, B02303. https://doi.org/10.1029/2003JB002607
McGuire, J. J., Wiens, D. A., Shore, P. J., & Bevis, M. G. (1997). The March 9, 1994 (*Mw* 7.6), deep Tonga earthquake: Rupture outside the seismically active slab. *Journal of Geophysical Research*, *102*(B7), 15,163–15,182.
Meng, L., Ampuero, J.-P., & Bürgmann, R. (2014). The 2013 Okhotsk deep-focus earthquake: Rupture beyond the metastable olivine wedge and thermally controlled rise time near the edge of a slab. *Geophysical Research Letters*, *41*, 3779–3785. https://doi.org/10.1002/2014GL059968

Myers, S. C., Wallace, T. C., Beck, S. L., Silver, P. G., Zandt, G., Vandecar, J., & Minaya, E. (1995). Implications of spatial and temporal development of the aftershock sequence for the *Mw* 8.3 June 9, 1994 deep Bolivian earthquake. *Geophysical Research Letters*, *22*(16), 2269–2272.

Ni, S., Kanamori, H., & Helmberger, D. (2005). Seismology: Energy radiation from the Sumatra earthquake. *Nature*, *434*(7033), 582–582.

Nissen, E., Elliott, J., Sloan, R., Craig, T., Funning, G., Hutko, A., et al. (2016). Limitations of rupture forecasting exposed by instantaneously triggered earthquake doublet. *Nature Geoscience*, *9*, 330–336.

Obara, K., Kasahara, K., Hori, S., & Okada, Y. (2005). A densely distributed high-sensitivity seismograph network in Japan: Hi-net by national research institute for earth science and disaster prevention. *Review of Scientific Instruments*, *76*(2), 021301. https://doi.org/10.1063/1.1854197

Ogawa, M. (1987). Shear instability in a viscoelastic material as the cause of deep focus earthquakes. *Journal of Geophysical Research*, *92*(B13), 13,801–13,810.

Okada, Y., Kasahara, K., Hori, S., Obara, K., Sekiguchi, S., Fujiwara, H., & Yamamoto, A. (2004). Recent progress of seismic observation networks in Japan—Hi-net, F-net, K-net and KiK-net. *Earth, Planets and Space*, *56*(8), xv–xxviii. https://doi.org/10.1186/BF03353076

Okuwaki, R., Yagi, Y., & Hirano, S. (2014). Relationship between high-frequency radiation and asperity ruptures, revealed by hybrid back-projection with a non-planar fault model. *Scientific Reports*, *4*, 7120.

Park, S., & Ishii, M. (2015). Inversion for rupture properties based upon 3-D directivity effect and application to deep earthquakes in the Sea of Okhotsk region. *Geophysical Journal International*, *203*(2), 1011–1025.

Peng, Z., Hill, D. P., Shelly, D. R., & Aiken, C. (2010). Remotely triggered microearthquakes and tremor in central California following the 2010 *Mw* 8.8 Chile earthquake. *Geophysical Research Letters*, *37*, l24312. https://doi.org/10.1029/2010GL045462

Persh, S. E., & Houston, H. (2004). Deep earthquake rupture histories determined by global stacking of broadband *P* waveforms. *Journal of Geophysical Research*, *109*, B04311. https://doi.org/10.1029/2003JB002762

Poli, P., & Prieto, G. (2014). Global and along-strike variations of source duration and scaling for intermediate-depth and deep-focus earthquakes. *Geophysical Research Letters*, *41*, 8315–8324. https://doi.org/10.1002/2014GL061916

Poli, P., & Prieto, G. A. (2016). Global rupture parameters for deep and intermediate-depth earthquakes. *Journal of Geophysical Research: Solid Earth*, *121*, 8871–8887. https://doi.org/10.1002/2016JB013521

Raleigh, C. B., & Paterson, M. (1965). Experimental deformation of serpentinite and its tectonic implications. *Journal of Geophysical Research*, *70*(16), 3965–3985.

Rost, S., & Thomas, C. (2002). Array seismology: Methods and applications. *Reviews of Geophysics*, *40*(3), 1008. https://doi.org/10.1029/2000RG000100

Satriano, C., Kiraly, E., Bernard, P., & Vilotte, J.-P. (2012). The 2012 *Mw* 8.6 Sumatra earthquake: Evidence of westward sequential seismic ruptures associated to the reactivation of a N-S ocean fabric. *Geophysical Research Letters*, *39*, L15302. https://doi.org/10.1029/2012GL052387

Silver, P. G., Beck, S. L., Wallace, T. C., Meade, C., Myers, S. C., James, D. E., & Kuehnel, R. (1995). Rupture characteristics of the deep Bolivian earthquake of 9 June 1994 and the mechanism of deep-focus earthquakes. *Science*, *268*(5207), 69–73.

Tibi, R., Bock, G., & Wiens, D. A. (2003). Source characteristics of large deep earthquakes: Constraint on the faulting mechanism at great depths. *Journal of Geophysical Research*, *108*(B2), 2091. https://doi.org/10.1029/2002JB001948

Tibi, R., Wiens, D. A., & Inoue, H. (2003). Remote triggering of deep earthquakes in the 2002 Tonga sequences. *Nature*, *424*(6951), 921–5.

Toda, S., Stein, R. S., Richards-Dinger, K., & Bozkurt, S. B. (2005). Forecasting the evolution of seismicity in southern California: Animations built on earthquake stress transfer. *Journal of Geophysical Research*, *110*, B05S16. https://doi.org/10.1029/2004JB003415

USGS (2018). U.S. Geological Survey. Earthquake hazards program.

Walker, K. T., Ishii, M., & Shearer, P. M. (2005). Rupture details of the 28 March 2005 Sumatra *Mw* 8.6 earthquake imaged with teleseismic *P* waves. *Geophysical Research Letters*, *32*, L24303. https://doi.org/10.1029/2005GL024395

Wang, D., Mori, J., & Uchide, T. (2012). Supershear rupture on multiple faults for the *Mw* 8.6 off northern Sumatra, Indonesia earthquake of April 11, 2012. *Geophysical Research Letters*, *39*, L21307. https://doi.org/10.1029/2012GL053622

Warren, L. M., Hughes, A. N., & Silver, P. G. (2007). Earthquake mechanics and deformation in the Tonga-Kermadec subduction zone from fault plane orientations of intermediate-and deep-focus earthquakes. *Journal of Geophysical Research*, *112*, B05314. https://doi.org/10.1029/2006JB004677

Warren, L. M., & Silver, P. G. (2006). Measurement of differential rupture durations as constraints on the source finiteness of deep-focus earthquakes. *Journal of Geophysical Research*, *111*, B06304. https://doi.org/10.1029/2005JB004001

Wei, S., Helmberger, D., Zhan, Z., & Graves, R. (2013). Rupture complexity of the *Mw* 8.3 Sea of Okhotsk earthquake: Rapid triggering of complementary earthquakes? *Geophysical Research Letters*, *40*, 5034–5039. https://doi.org/10.1002/grl.50977

Wei, S. S., Wiens, D. A., van Keken, P. E., & Cai, C. (2017). Slab temperature controls on the Tonga double seismic zone and slab mantle dehydration. *Science Advances*, *3*(1), e1601755.

Wiens, D. A. (2001). Seismological constraints on the mechanism of deep earthquakes: Temperature dependence of deep earthquake source properties. *Physics of the Earth and Planetary Interiors*, *127*(1-4), 145–163.

Wiens, D. A., & Gilbert, H. J. (1996). Effect of slab temperature on deep-earthquake aftershock productivity and magnitude–frequency relations. *Nature*, *384*(6605), 153–156.

Wiens, D. A., Gilbert, H., Hicks, B., Wysession, M., & Shore, P. (1997). Aftershock sequences of moderate-sized intermediate and deep earthquakes in the Tonga subduction zone. *Geophysical Research Letters*, *24*(16), 2059–2062.

Wiens, D. A., & McGuire, J. J. (1995). The 1994 Bolivia and Tonga events: Fundamentally different types of deep earthquakes? *Geophysical Research Letters*, *22*, 2245–2248.

Wiens, D. A., & McGuire, J. J. (2000). Aftershocks of the March 9, 1994, Tonga earthquake: The strongest known deep aftershock sequence. *Journal of Geophysical Research*, *105*(B8), 19,067–19,083.

Wiens, D. A., McGuire, J. J., & Shore, P. J. (1993). Evidence for transformational faulting from a deep double seismic zone in Tonga. *Nature*, *364*(6440), 790–193.

Wiens, D. A., McGuire, J. J., Shore, P. J., Bevis, M. G., Draunidalo, K., Prasad, G., & Helu, S. P. (1994). A deep earthquake aftershock sequence and implications for the rupture mechanism of deep earthquakes. *Nature*, *372*(6506), 540–543.

Wiens, D. A., & Snider, N. O. (2001). Repeating deep earthquakes: Evidence for fault reactivation at great depth. *Science*, *293*(5534), 1463–1466.

Xu, Y., Koper, K. D., Sufri, O., Zhu, L., & Hutko, A. R. (2009). Rupture imaging of the *Mw* 7.9 12 May 2008 Wenchuan earthquake from back projection of teleseismic *P* waves. *Geochemistry, Geophysics, Geosystems*, *10*, Q04006. https://doi.org/10.1029/2008GC002335

Yagi, Y., Nakao, A., & Kasahara, A. (2012). Smooth and rapid slip near the Japan trench during the 2011 Tohoku-oki earthquake revealed by a hybrid back-projection method. *Earth and Planetary Science Letters*, *355*, 94–101. https://doi.org/10.1016/j.epsl.2012.08.018

Ye, L., Lay, T., Kanamori, H., & Koper, K. D. (2013). Energy release of the 2013 *Mw* 8.3 sea of Okhotsk earthquake and deep slab stress heterogeneity. *Science*, *341*(6152), 1380–1384.

Zhan, Z. (2017). Gutenberg–Richter law for deep earthquakes revisited: A dual-mechanism hypothesis. *Earth and Planetary Science Letters*, *461*, 1–7.

Zhan, Z., Kanamori, H., Tsai, V. C., Helmberger, D. V., & Wei, S. (2014). Rupture complexity of the 1994 Bolivia and 2013 Sea of Okhotsk deep earthquakes. *Earth and Planetary Science Letters*, *385*, 89–96.